Refinements to Ice Particle Mass Dimensional and Terminal Velocity Relationships for Ice Clouds. Part I: Temperature Dependence

ANDREW J. HEYMSFIELD AND AARON BANSEMER

National Center for Atmospheric Research, Boulder, Colorado*

CYNTHIA H. TWOHY

College of Oceanic and Atmospheric Sciences, Oregon State University, Corvallis, Oregon

(Manuscript received 10 April 2006, in final form 17 July 2006)

ABSTRACT

This two-part study attempts to find appropriate mass dimension and terminal velocity relationships that, when considered together with particle size distributions (PSD), agree with coincident measurements of ice water content (IWC), and with variables related to higher moments such as the mean mass-weighted fall speed. Reliable relationships are required for improving microphysical parameterizations for weather forecast models and developing methods for evaluating them, subjects addressed in detail in Part II of this study.

Here, a range of values from 1.5 to 2.3 is assumed for the exponent b in the mass dimension relationship, $m = aD^b$, where D is the maximum particle dimension, to bound its likely value for sizes above about 100 μm. Measured IWC and size spectra are used to find appropriate values for the coefficient a. It is demonstrated that all values of the exponent b, with appropriate a coefficients, can fit the IWC measurements. Coincident information on particle cross-sectional areas with the $m(D)$ relationships is used to develop general fall velocity relationships of the form $V_t = AD^B$. These assessments use five midlatitude, synoptically generated ice layers, and 10 low-latitude, convectively generated ice cloud layers, spanning the temperature range from $-60°$ to 0°C.

The coefficients a and A and exponent B are represented in terms of the exponent b and are shown to be temperature-dependent for the synoptic clouds and relatively independent of it in the convective clouds, a result of particle mixing through the cloud column. Consistency is found with earlier results and with analytic considerations. It is found that the fall velocity is inversely proportional to the air density to approximately the exponent 0.54, close to values assumed in earlier studies.

1. Introduction

In general circulation models (GCMs), the treatment of ice clouds requires better descriptions of the microphysical properties of the cloud layers. Much of what has been learned about ice clouds in general comes from measurements from relatively few locations, primarily in the Northern Hemisphere. CloudSat, a millimeter wavelength (95 GHz) radar and the Cloud–Aerosol Lidar and Infrared Pathfinder Satellite Observation Satellite (CALIPSO), a dual wavelength lidar system (0.532 and 1.064 μm), now collecting data, present new opportunities to characterize the microphysical properties of ice clouds on a global scale.

In models from weather forecasting (Lin et al. 1983; Rutledge and Hobbs 1984, hereafter RH84) to GCMs (Fowler et al. 1996), parameters for the microphysical properties of ice and snow are necessary in representing clouds and precipitation. In a basic form, these parameters would include the total ice particle concentration (N_t) and a mean ice particle density ($\overline{\rho_e}$). More elaborate schemes would include the ice particle concentration (N) as a function of particle maximum dimension (D) for the ice particle size distribution as well as ice particle areas and mass dimensions, $A(D)$ and $m(D)$. These parameters may then be used to determine many microphysical properties: extinction (a function, f of $[N(D)A(D)]$), ice water content (IWC, $f[N(D)m(D)]$),

* The National Center for Atmospheric Research is sponsored by the National Science Foundation.

Corresponding author address: Andrew Heymsfield, National Center for Atmospheric Research, 3450 Mitchell Lane, Boulder, CO 80301.
E-mail: heyms1@ucar.edu

DOI: 10.1175/JAS3890.1

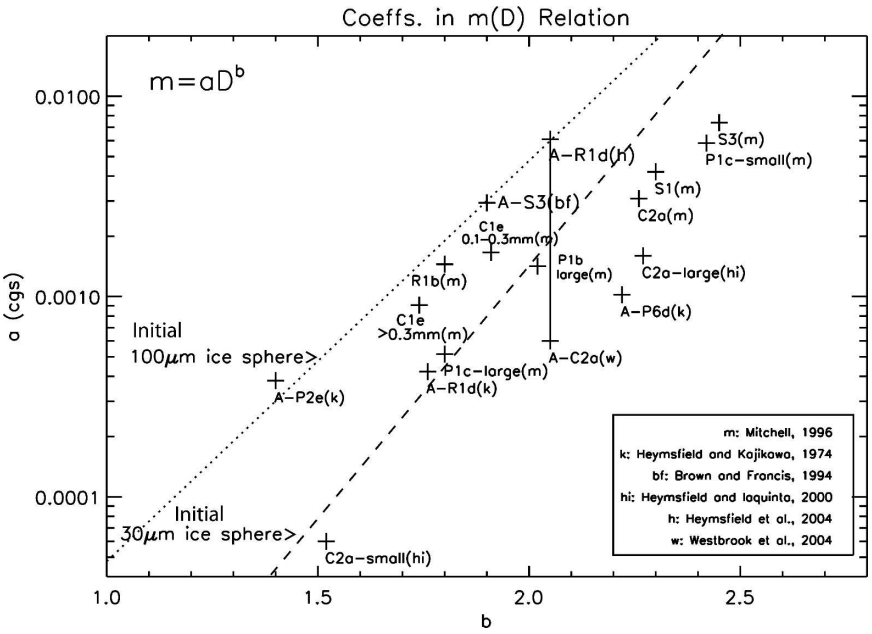

FIG. 1. Coefficients in $m(D)$ relationships from a number of studies involving surface collected ice particles, analytical models, and in situ data. Habit codes for each data point are from Magono and Lee (1966). "Large" indicates coefficients that represent sizes above several hundred microns. The dotted and dashed curves indicate the values of a and b derived using a threshold D_t for an ice sphere of 100 and 30 microns, respectively, as described in the text.

equivalent radar reflectivity (Z_e, $f[N(D)m^2]$), distribution of particle fall velocity with size ($V_t = f[m(D)/A(D)]$), population mean mass-weighted fall speed ($V_m = f[V_t(D)m(D)/\text{IWC}]$), and reflectivity-weighted fall speed ($V_Z = f[V_t(D)Z_e(D)/Z_e]$). For a given particle size, the mass of individual ice particles varies from cloud to cloud (Atlas et al. 1995). Presently available airborne probes cannot measure the mass of individual cloud particles. Although a number of researchers have reported $m(D)$ relationships that work well in providing estimates of IWC from a range of power-law type calculations, they may not provide accurate estimates of the higher moments (e.g., Z_e).

The presently reported two-part study is built on the earlier work of Brown and Francis (1995, hereafter BF95), Heymsfield (2003, hereafter H03), and Heymsfield et al. (2004, hereafter H04). These investigators used both PSD and direct measurements of IWC to evaluate or estimate $m(D)$ relationships. The goal of the present study is to develop $m(D)$ relationships that work well for lower moments such as the IWC as well as higher moments of the PSD such as V_m and Z_e. Given the need for accurate estimates of the higher moments in GCMs, the work is especially important as well for forthcoming spaceborne-radar investigations. Part I examines the temperature dependence of mass-dimensional and terminal velocity relationships in a range of cloud types and discusses how the results may relate to the nucleation and growth of ice particles. A range of such relationships that reproduce the measured IWC have been derived. However, we are unable to determine from this analysis which relationships produce more accurate estimates of the higher moments. This is determined in Heymsfield et al. (2007, hereafter Part II).

Most previous investigations have represented mass-dimensional relationships to be power laws of the form

$$m = aD^b, \tag{1}$$

which gives the mass of an ice particle in terms of a coefficient, a, and an exponent, b. The value for b may range from about 1.5 for very thin dendritic crystals to 3.0 for solid ice spheres. Figure 1 gives the values for a and b from a number of studies that included a range of single particle habits and of aggregates of such single particles, the latter labeled A– in the figure. Because not much is known about the coefficients for particles below about 100 μm, values are not shown for them in Fig. 1; however, b should be close to that for ice spheres. In Fig. 1, the spread in the coefficient a is greater than an order of magnitude whereas exponent b varies less, being usually above 2.0 for single crystals and about 2.0 for aggregates. Since planar crystals contribute most to snowfall at the ground, they also domi-

nate the reports. Most of the studies derived mass and maximum dimension from only a few tens of collected particles. One or more $m(D)$ relationships were then fitted to the data to represent single particle types of all sizes. Particles collected at the ground range in size from hundreds of microns to a few millimeters, therefore each reported relationship covers a restricted size range, usually hundreds of microns or larger and, since they are often collected on different days, may not be representative of any cloud or day. Besides power-law parameterizations for size-to-mass conversion, there are ones using perimeter, area, and linear size of 2D images of ice particles. One such study was recently reported by Baker and Lawson (2006).

Particle ensembles usually comprise a multitude of habits, many irregular, and contain thousands or more particles per cubic meter. Because of these facts, BF95, Heymsfield and Iaquinta (2000), H04, and Westbrook et al. (2004) evaluated or developed $m(D)$ relationships based upon aircraft PSDs or, in some cases, from direct measurements of IWCs. Locatelli and Hobbs (1974) derived a relationship for 19 unrimed aggregates of cold temperature crystals with D from 0.1 to 0.3 cm, collected at the ground. In evaluating this relationship, BF95 applied the fitted relationship, $m = 0.002\,94\,D^{1.9}$ (cgs units, where D is in centimeters), to PSD and IWC in situ measurements acquired in two cirrus flights. The relationship was used for all particles larger than 90 μm in diameter, where the density implied by the relationship is $\leq$0.91 g cm^{-3}, the density of solid ice. For D below the threshold diameter, $D_t < 90$ μm, the density was taken as 0.91 g cm^{-3}. Heymsfield and Iaquinta (2000) used an analytic model of the dominant cirrus crystal type, bullet rosettes, to express the mass in terms of the projected cross-sectional area that can be measured from airborne imaging probe particle spectrometers. This approach was used in several cirrus clouds where bullet rosettes dominated the IWC, and found that exponent b was 1.5 for small rosettes and about 2.2 for larger ones. In these clouds, rosette aggregates, larger than 800 μm were few and contributed less to the IWC than did the single ones. Westbrook et al. (2004) used theoretical and computer models to show that the aggregates of bullet rosettes that were found in the cirrus studied by Heymsfield and Iaquinta scaled as fractal particles and concluded that b, given by the vertical line in Fig. 1 herein, was about 2.05. They did not derive a value for coefficient a. The PSD and IWC measured from low-latitude, convectively generated, ice cloud layers were used by H04 to estimate the population-mean, ice particle density, and an $m(D)$ relationship that fit the measured IWC, of $m = 0.0061D^{2.05}$. Although all of the b values, from 1.8 to 2.4, could have matched the observed IWC, an exponent b of 2.05 fit the data with the lowest standard deviation of the estimated error in IWC. More recently, Heymsfield et al. (2005) have shown that a single $m(D)$ relationship, with an exponent b of about 2.0, cannot simultaneously provide both accurate measurements of IWC and radar reflectivity. It yielded the correct IWC but too large a Z_e, indicating that too much mass is given to the larger particles. They found that an exponent b of about 1.6, giving smaller mass to the larger particles and a larger mass to the smaller ones, assured quite accurate estimates of IWC and Z_e.

The cloud microphysics community has devoted considerable attention toward characterizing the terminal velocities of ice particles as a function of size for given habits from measurements obtained at the ground. These studies have been useful for obtaining drag coefficients and estimates of the values of variables A and B in $V_t = AD^B$. However, they are of limited generality because they contained some of the same limitations as was noted above for ice particle mass with the additional limitations that mass was usually not measured and adjustments for pressure levels above the surface could not be accurately obtained. H03 derived values for A and B for midlatitude and tropical ice clouds in terms of the slope of gamma PSD (λ) fitted to the measurements. Ice particle mass was estimated from ice particle cross-sectional area and particle diameter, with the mean value of b for the midlatitude and tropical clouds of 2.3 $\pm$ 0.06 and 1.95 $\pm$ 0.1, respectively. A representation to adjust the fall speed for height in the atmosphere was developed. Parts I and II of the present study will refine the estimates of A and B and represent them in terms of temperature.

Because it is important to accurately represent IWC, V_m, and Z_e, $m(D)$ relationships should be evaluated on how well they yield a range of moments. With a single $m(D)$ relationship, many properties of ice clouds may be analytically derived for a given PSD, however, it is desirable to find a relationship that covers the PSD's size range. Because different processes such as diffusional/aggregational growth lead to different $m(D)$ relationships, a single relationship is obviously an oversimplification. With this goal in mind, however, certain guidelines may aid the process. At the small end of a single power-law type $m(D)$, one anchor for the $m(D)$ relationship is given by the size, D_p, at which an ice particle begins to take on a nonspherical shape and its mass is less than that of an equivalent diameter ice sphere. This occurs at the threshold diameter where the density implied by the $m(D)$ relationship equals

0.91 g cm^{-3}: $D_t = (6a/0.91\pi)[1/(3 - b)]$. Below D_t, the density is approximately 0.91 g cm^{-3}. Through heterogeneous ice nucleation, drop sizes at the point of freezing, on average, are likely to diminish with temperature. We predict from theory that the lower the temperature below about −37°C, the smaller the size of a homogeneously frozen haze particle or droplet. Therefore, D_t is likely to decrease with temperature, implying that a will also decrease with temperature. The largest particles in a distribution give an anchor point at the large end of the PSD. Many observations show maximum particle size increasing with temperature, therefore, the anchor point at the large end of the PSD increases with temperature. A single $m(D)$ relationship with fixed b shifts, therefore, to lower a with decreasing temperature. By setting mass m in Eq. (1) to be consistent with D_t of 30 or 100 μm, the coefficient a may be found as a function of b. The a, b coefficients for these two sizes would then fall along the sloping lines shown in Fig. 1. The sloping lines have two implications: first, they bound the results found from earlier studies. Second, because D_t should increase with temperature, they suggest that the coefficient a increases with temperature.

For ice clouds formed through large-scale uplift and deep convection, Part I uses in situ measurements of PSD and IWC over a wide range of temperatures to derive a range of $m(D)$ to provide accurate estimates of IWC and $V_t(D)$. Sources for the data are discussed in section 2, the methodology in section 3, and section 4 gives an assessment of the significance of the results. The primary conclusions are given in section 5.

2. Data sources

This study draws upon in situ measurements acquired between −60° and 0°C in middle- and low-latitude ice cloud layers. The datasets used were chosen because PSD and direct measurements of IWC were available. The data sources and collection methods are reviewed in what follows.

Cloud layers referred to as synoptically generated were sampled in midlatitudes on five different days in two different projects. Three cirrus layers were sampled during an intensive field operation in March 2000, over the Southern Great Plains (SGP) Atmospheric Radiation Measurement site (ARM). The ARM dataset was collected by the University of North Dakota (UND) Citation aircraft with vertically pointing radars. Each of these clouds was comprised of bullet-rosette-type crystals (see Fig. 2). On 5 March, the cirrus were part of a jet stream band; on 9 March they formed in generating cells (Heymsfield an Iaquinta 2000), and on 13 March were more stratiform. These clouds were sampled between −52° and −25°C. On 12 March, a deep layer cloud was sampled between −30° and 0°C. This cloud was comprised of crystals with complex shapes, many displaying evidence of initiation at cirriform temperatures (Fig. 3). There were two brief encounters with liquid water (LW) as determined from a Rosemount icing probe with a detection threshold of about 0.01 g m^{-3}; these periods were not used.

During the Alliance Icing Research Study II (AIRS) in 2003 (Isaac et al. 2005), a deep cloud layer with embedded convection was sampled on 19 November 2003 from the National Center for Atmospheric Research (NCAR) C-130. The aircraft, centered on the 35 GHz, McGill radar at Mirabel Airport near Montreal, flew five descending and ascending spirals through the ice cloud layer. Supercooled liquid water was detected intermittently with a King LW probe, primarily at temperatures between 0° and −5°C. Periods where the liquid water content exceeded about 0.05 g cm^{-3} were not used in the analysis. The aircraft cloud particle imager (CPI) probe data showed a multitude of crystal types and supercooled liquid water throughout the spirals: at temperatures warmer than −8°C, single crystals, including needles; at lower temperatures, capped columns and planar crystals, and aggregates at all levels. During the Cirrus Regional Study of Tropical Anvil and Cirrus Layers: Florida Area Cirrus Experiment (CRYSTAL FACE) in 2002, the UND Citation made 10 flights, sampling between −60° and 0°C, primarily in convectively generated, low-latitude ice cloud layers. The LW occurrence, as detected by a Rosemount icing probe, was essentially nonexistent.

For particles from about 50 to 1000 μm, size and cross-sectional area were obtained from Particle Measuring System (PMS) 2D-C probes with a resolution of about 33 μm and a threshold detection size of about twice that. For precipitation-sized particles in the ARM flights, the PMS 2D-P was used except on 5 March. Fortunately, the 5 March case had few >500-μm particles. The probe sizes from 1000 μm to more than 3 mm. For CRYSTAL and AIRS-2, a Stratton Park Engineering Company (SPEC) high-volume precipitation spectrometer, a 2D probe with a resolution of 200 μm (HVPS) collected data from 200 μm to above 1 cm. Particles objectively determined to be shattered on the tips of the 2D probes have been removed (Field. et al. 2006). For particles ranging from 2 to about 50 μm, size distributions were obtained from a forward scattering spectrometer probe (FSSP); however, large particles may be broken up in the probe's inlet and may have led to overcounting in cases on 12 March and 19 November and in CRYSTAL. At low resolution, particle shape

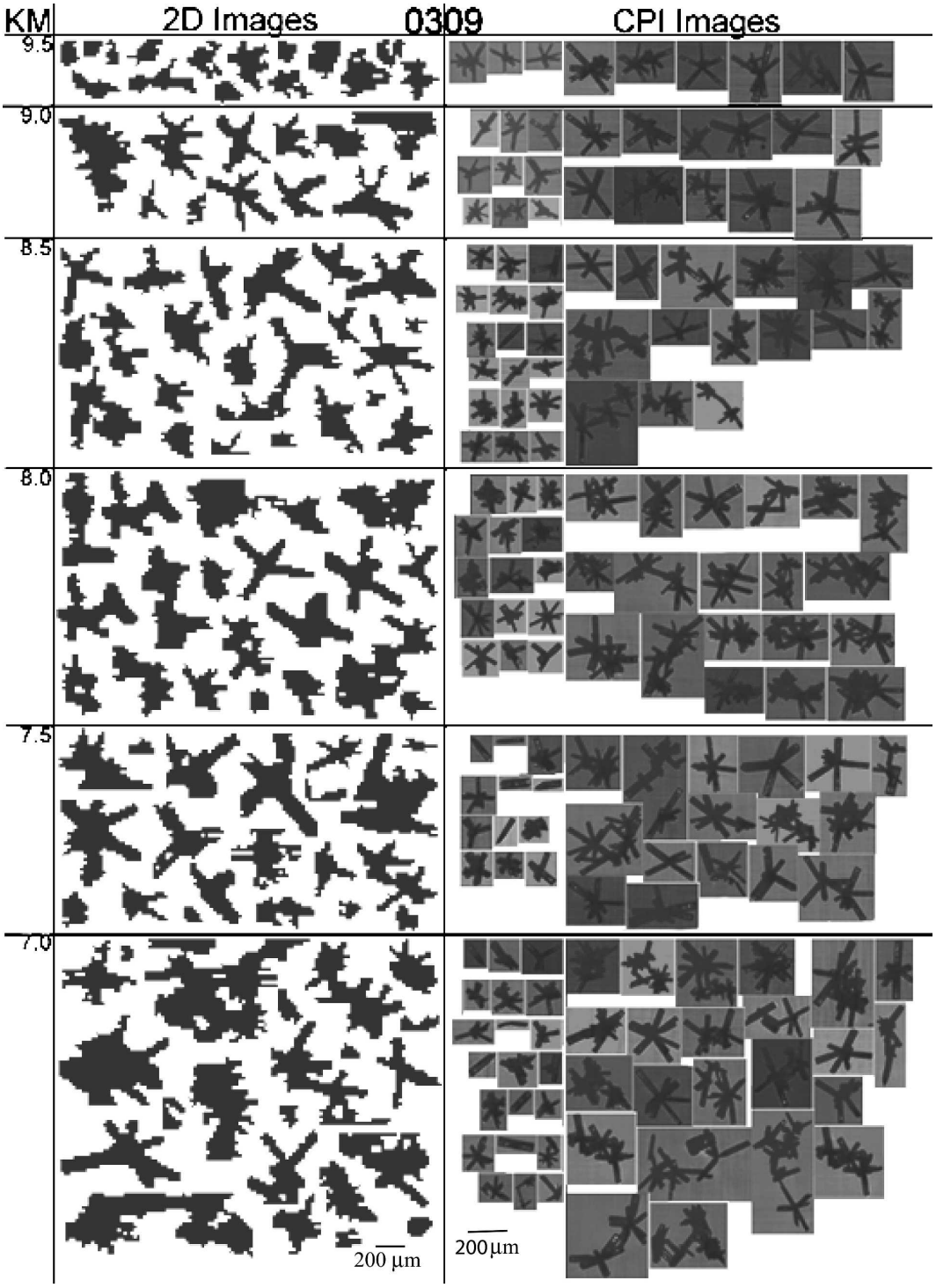

FIG. 2. Vertical distribution of particles on 9 March from (left) the 2D-C probe and (right) cloud particle imager probe.

and area were obtained by the 2D and HVPS probes and, at higher resolution with a CPI probe (Figs. 2 and 3). The PSD data were averaged over 5-s intervals or about 1 km of horizontal flight and binned into 33 intervals for the imaging probes and 15 for the FSSP. During all three field programs, a counterow virtual impactor (CVI; Twohy et al. 1997) directly measured the condensate mass above a threshold particle size of

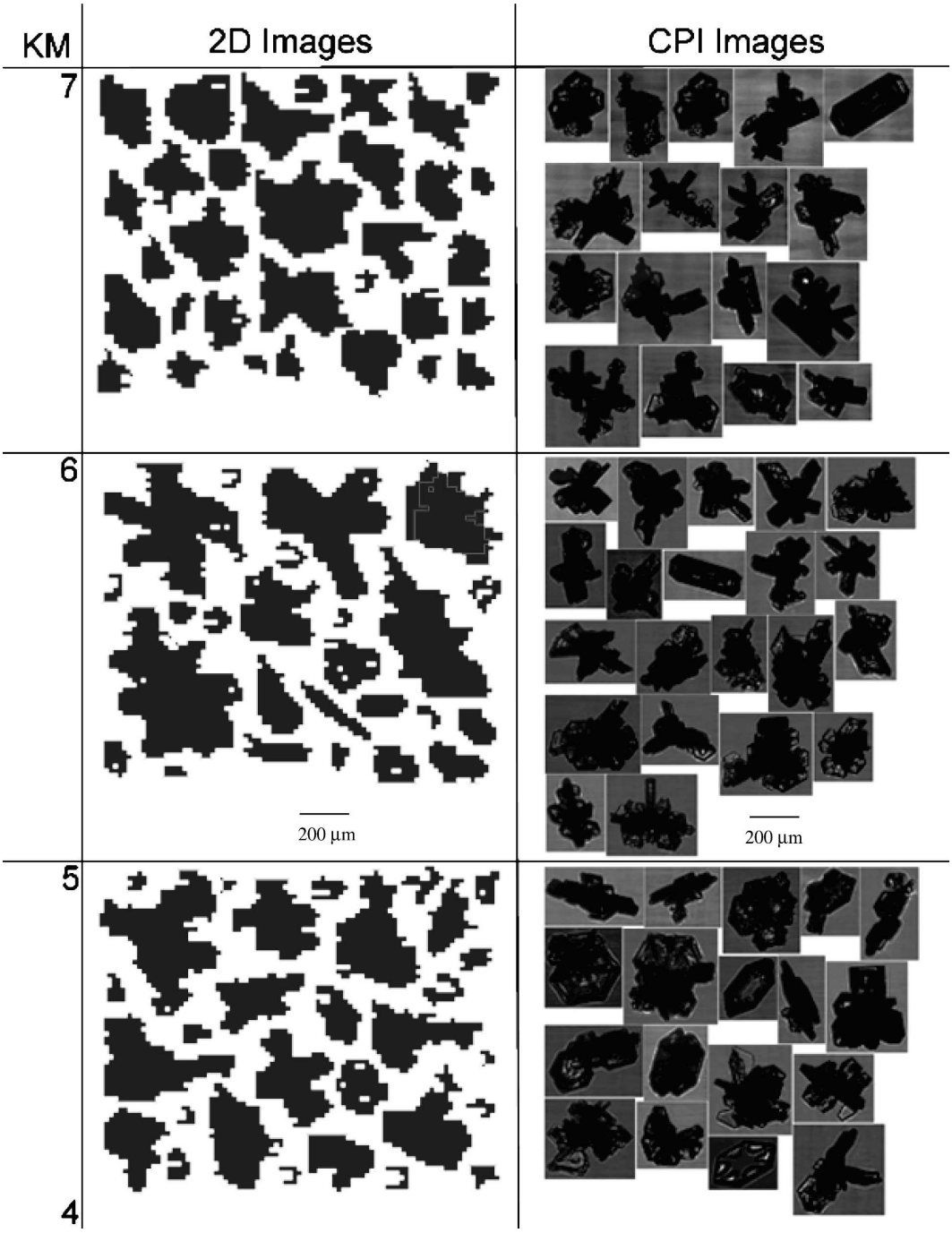

FIG. 3. As in Fig. 2, but for 12 March 2000.

about 6–8 μm in diameter. The appendix describes the instrument technique and its expected uncertainty, which is less than 16% for CVI IWCs larger than 0.01 g m^{-3}. IWCs were not used below 0.01 g m^{-3}, since below that value, uncertainty increases due to variations in the out-of-cloud baseline signal and due to hysteresis in the sample line.

3. Methodology

As noted in the introduction, a range of (a, b) values in Eq. (1) can give the correct IWC for a given PSD. In this section the combination of these coefficients yielding correct IWCs and particle bulk densities are derived for ice clouds, from synoptically generated cirrus to lay-

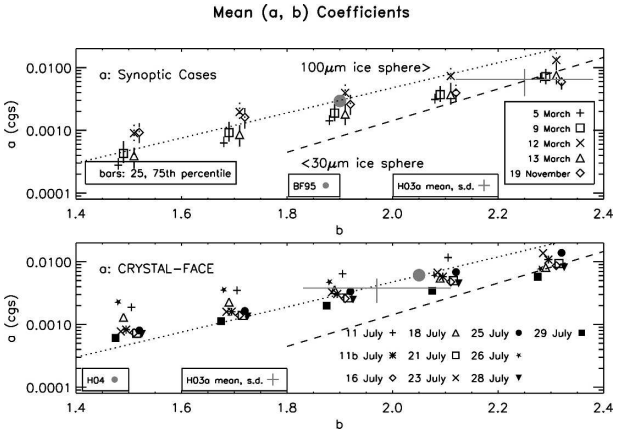

FIG. 4. Logarithmically weighted, mean values for coefficient *a* in mass-dimensional relationships, as a function of exponent *b*: (a) five midlatitude synoptically generated ice clouds; (b) CRYSTAL FACE clouds. The dotted and dashed curves indicate the values of *a* and *b* derived using a threshold D_t for an ice sphere of 100 and 30 μm, respectively, as in Fig. 1.

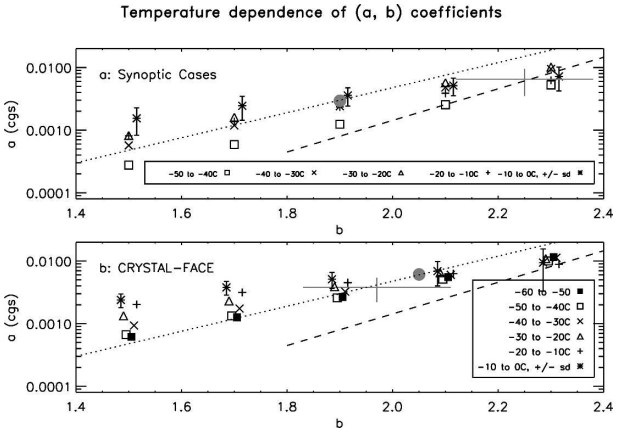

FIG. 5. Mean values of coefficient *a* for each exponent *b,* subdivided by temperature, for (a) synoptic cases, (b) CRYSTAL FACE. Large symbols same as in Fig. 4.

ers formed through deep convection. Temperature dependence is also examined. The analysis used data from ice cloud layers formed on 15 days.

a. Ice particle mass coefficients

In Eq. (1), in order to span its probable range, the exponent *b* varies from 1.5 to 2.3 (Fig. 1). For values of *b* in the given range, values of *a* are derived for each 5 s PSD (obtained from FSSP and 2-D probes) such that the IWC obtained by summation of the PSD yields the IWC measured by the CVI. For particles from the FSSP, there is almost no information as to their mass. Balloon-borne replicator observations indicate that particles with maximum diameters 50 μm and below have cross-sectional areas that are 80% or more of the cross-sectional areas of spheres (Heymsfield and Miloshevich 2003). Replicator particles sized 10 to 20 μm are essentially spherical (Zhang et al. 2004). Using the particle images from a CPI, Korolev and Isaac (2003) reached a similar conclusion: ice particles of diameters 50 μm and below have cross-sectional areas more than 80% as large as spheres. For simplicity, therefore, all FSSP particles are assumed to be solid ice spheres. This assumption produces little error in estimates of IWC (see also H04). Probe detection thresholds, and errors and uncertainties resulted in periods that were omitted from the dataset. This is discussed in more detail in the last part of the appendix.

For the five synoptic cloud case studies, Fig. 4a shows that coefficient *a* increases with increasing exponent *b*. Nearly the same value for *a* occurs in the three cirrus cases as well (5, 9, and 13 March). These results are consistent for bullet rosettes (Fig. 2), the predominant particle in these cases and in most synoptically generated cirrus. The mean values of (*a, b*) derived by H03, based on analytic representations for bullet rosettes by Heymsfield and Iaquinta 2000), conform closely to the mean values for the larger values of *b* found here (Fig. 4a). For the warmer cases on 12 March and 19 November, the coefficient *a* is almost twice those of the cirrus cases, indicating particles of higher bulk densities (Fig. 2 versus Fig. 3). Values from BF95 are above those for cirrus and close to those for the two warmer cases. For CRYSTAL FACE the *a* coefficients (Fig. 4b) are almost cloud-independent and similar to the warmer synoptic cases on 12 March and 19 November. The mean (*a, b*) values derived by H04 for the CRYSTAL FACE dataset fall in line with the values found here. The range of values found by H03 for the Tropical Rainfall Measurement Mission (TRMM) field campaign dataset lies slightly below the line; this is consistent with the TRMM observations wherein the particles were considerably less rimed than those sampled during CRYSTAL FACE.

As shown in Fig. 5a, coefficient *a* increases steadily with increasing temperature for the synoptic cases, which may account for its larger values in warmer clouds. For the highest temperature range, coefficients for BF95 and H03 coincide with observations. For CRYSTAL FACE; however, the coefficients show less of a temperature dependence (Fig. 5b).

Figure 6 gives *a* for specific values of *b* as a function of temperature, segregated by synoptic and CRYSTAL FACE datasets. In this figure, linear least squares curves are fitted to the data and the coefficients for the curve fits are given in Table 1. The horizontal distance flown by the aircraft for each flight and temperature

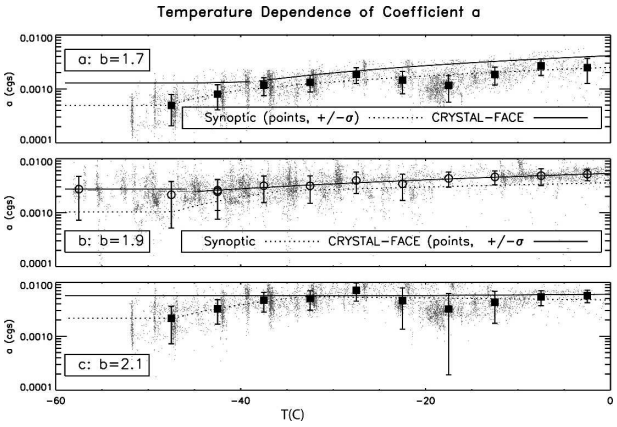

FIG. 6. As in Fig. 5, for three b values. (a), (c) Synoptic cases, showing points for each PSD, mean values (solid rectangles) and standard deviations and (b) CRYSTAL FACE cases, points, mean values (open circles), and standard deviations. Linear curves are plotted to data from above and below about −20°C, with the exception of the synoptic cases where, above about −20°C, a mean value has been used.

interval is listed in Table 2. The following conclusions may be drawn from Fig. 6 and Table 2:

- In CRYSTAL FACE clouds the coefficient a is nearly independent of temperature and is relatively constant for b's of 2.0 and larger whereas, and especially below −25°C, there is a marked dependence on temperature in synoptic clouds.
- For the case on 19 November, the dip in a near −20°C (Figs. 6a,c) occurs from the predominance of lower density, single and aggregated dendritic crystals, presumably lofted upward in convection. At similar temperatures, the particles sampled on 12 March were higher density, spatial crystals. This demonstrates the effects of habit variability.
- For synoptic cases, with $b = 1.9$, as in BF95, at 0°C, the curve has an intercept of about 0.0035 (cgs units), close to their value of 0.00294. However, for the CRYSTAL FACE clouds, it is much larger, 0.005 25.
- For the CRYSTAL FACE dataset, H04 tested constant, temperature-independent values for a and b. The combination, (0.0061, 2.05) produced the smallest standard deviation of the IWC (parameter)/IWC (CVI). The smallest standard deviation occurs when a is essentially independent of temperature. Here, as shown in Fig. 6, this is where $b = 2.1$. Even so, (a, b) from 1.5 to 2.3 would have produced an equally accurate IWC and, for the higher moments, some value within that range might have produced better results. The H04 value for a of 0.0061 (cgs) is the nearly the same value at 0°C given in Fig. 6c herein, although H04 found b to be 2.05, not 2.1.
- For the ARM dataset, H04 found the exponent b giving the lowest standard deviation was 2.4. Although it is not shown for $b = 2.4$ in Fig. 6, examination of the data shows that this result occurs for the same reason as in CRYSTAL FACE: a is essentially independent of temperature for $b = 2.4$.
- There is a good sampling of each temperature interval on a number of days, improving the reliability of the results.

TABLE 1. Temperature dependence of a coefficient for curve fits of synoptic and CRYSTAL FACE [a(cgs) = $C_0 + C_1T$] cases. Temperature (T) is given in °C, and there are two curve fits given for each b, above and below T_{lim}; value of a below −50°C (synoptic) and −60°C CRYSTAL FACE, a_{rmin}, is shown for each b.

Curve	$b = 1.5$	1.7	1.9	2.1	2.3
Synoptic					
T_{lim} (°C)	All T	−39.9	−35.3	−33.2	−32.3
$\leq T_{lim}$					
C_0	0.001 61	0.003 24	0.006 93	0.013 16	0.023 43
C_1	0.000 028 8	0.000 057 4	0.000 124 9	0.000 233 1	0.000 398
$> T_{lim}$					
C_0	0.001 61	0.002 52	0.003 58	0.004 71	0.005 46
C_1	0.000 032 2	0.000 039 1	0.000 029 8	−0.000 215	−0.000 157 9
a_{rmin}	0.000 23	0.000 50	0.001 03	0.00215	0.004 49
CRYSTAL FACE					
T_{lim} (C)	−40.5	−37.2	−46.3	All T	−23.7
$\leq T_{lim}$					
C_0	0.000 70	0.002 10	0.001 84	0.006 30	0.007 95
C_1	0.000 002 7	0.000 017 2	−0.000 012 8	0.000 015 5	−0.000 054 6
$> T_{lim}$					
C_0	0.002 81	0.004 13	0.005 3	0.006 3	0.006 83
C_1	0.000 054 6	0.000 071 9	0.000 061 8	0.000 015 5	−0.000 101 9
a_{rmin}	0.000 59	0.001 28	0.002 72	0.005 69	0.011 93

TABLE 2. Integrated in-cloud horizontal flight length (km) from CVI, above its detection threshold.

Synoptic						
Temperature range (°C)	5 Mar 2000	9 Mar 2000	12 Mar 2000	13 Mar 2000	19 Nov 2003	Total (km)
−55 to −50	30 (km)	0	0	205	0	235
−50 to −45	84	224	0	264	0	572
−45 to −40	78	265	0	181	0	525
−40 to −35	72	243	0	548	0	864
−35 to −30	0	197	162	396	0	756
−30 to −25	0	80	174	45	2	302
−25 to −20	0	2	214	44	213	474
−20 to −15	0	0	237	28	753	1019
−15 to −10	0	0	140	0	278	419
−10 to −5	0	0	37	1	118	156
−5 to 0	0	0	29	0	33	63

CRYSTAL FACE											
Temperature range (°C)	11 Jul 2002	11 Jul 2002 (b)	16 Jul 2002	18 Jul 2002	21 Jul 2002	23 Jul 2002	25 Jul 2002	26 Jul 2002	28 Jul 2002	29 Jul 2002	Total (km)
−55 to −50	0	151	0	0	7	38	119	0	0	137	453
−50 to −45	0	71	369	0	66	279	80	0	0	119	986
−45 to −40	0	68	226	63	110	53	141	0	4	228	897
−40 to −35	0	95	215	109	182	146	93	0	46	81	973
−35 to −30	0	175	213	126	82	100	79	0	101	81	959
−30 to −25	0	278	102	48	32	25	31	0	5	78	603
−25 to −20	0	21	88	147	42	19	33	0	9	61	422
−20 to −15	8	4	25	73	0	15	16	0	0	0	144
−15 to −10	26	7	2	60	0	0	0	205	0	0	303
−10 to −5	157	0	2	62	0	5	0	273	0	0	501
−5 to 0	6	0	0	7	0	0	0	281	0	2	297

- These average coefficients can be fed back into the dataset to provide estimates of the a coefficient from temperature for periods when the IWC are below the CVI's detection threshold or when there are other probe errors.

b. Ice particle density

The ice particle bulk or effective density, ρ_e, may be derived from the ratio of the ice particle mass divided by the volume of a sphere of diameter, D:

$$\rho_e(D) = \left(\frac{6a}{\pi}\right) D^{b-3}. \quad (2)$$

Using the synoptically generated ice cloud observations on 9 March as an example for cold temperatures, in Fig. 7, single points indicate ρ_e at the maximum particle size for each PSD. The decrease of ρ_e with size is due to the more complex crystal shapes that tend to be present at larger sizes, which deviate substantially from spherical. Increasing exponent b reduces ρ_e for smaller particles and increases it for larger ones. These results are also illustrated by the dashed and dotted lines in Figs. 4a,b.

Figure 7 gives a curve derived from $\rho_e = \bar{a}D^{(b-3)}$, where $\bar{a}$ is the mean value of a for the 9 March case given in Fig. 4a. Dotted curves in each panel in Fig. 7 show the fit to the data. The mean and fitted curves agree well, indicating that a single $\rho_e - D$ or $m - D$ curve, a single value for exponent b, adequately represents all the data in this case. There is no indication that two curves are necessary. Furthermore, it would appear likely that the densities, for those cases with IWC below the CVI detection threshold, would also fall along the same lines.

Figure 7 also shows curves derived using coefficient a for the warmer 12 March case from Fig. 5. Here ρ_e is considerably larger than for 9 March, which is consistent with the visual inspection of the particles sampled for these cases (see Figs. 2 and 3). Curves for the CRYSTAL FACE cases are similar to those for 12 March.

The average value for ρ_e of 0.1 g cm^{-3} used by Lin et al. (1983, hereafter L83) and RH84) one-moment ice microphysical parameterization clearly does not reflect the ρ_e size dependence shown in Fig. 7. This dependence is even more clearly illustrated in Fig. 8, in which the population mean densities, ρ_e, are given for the synoptic and CRYSTAL FACE datasets as a function of

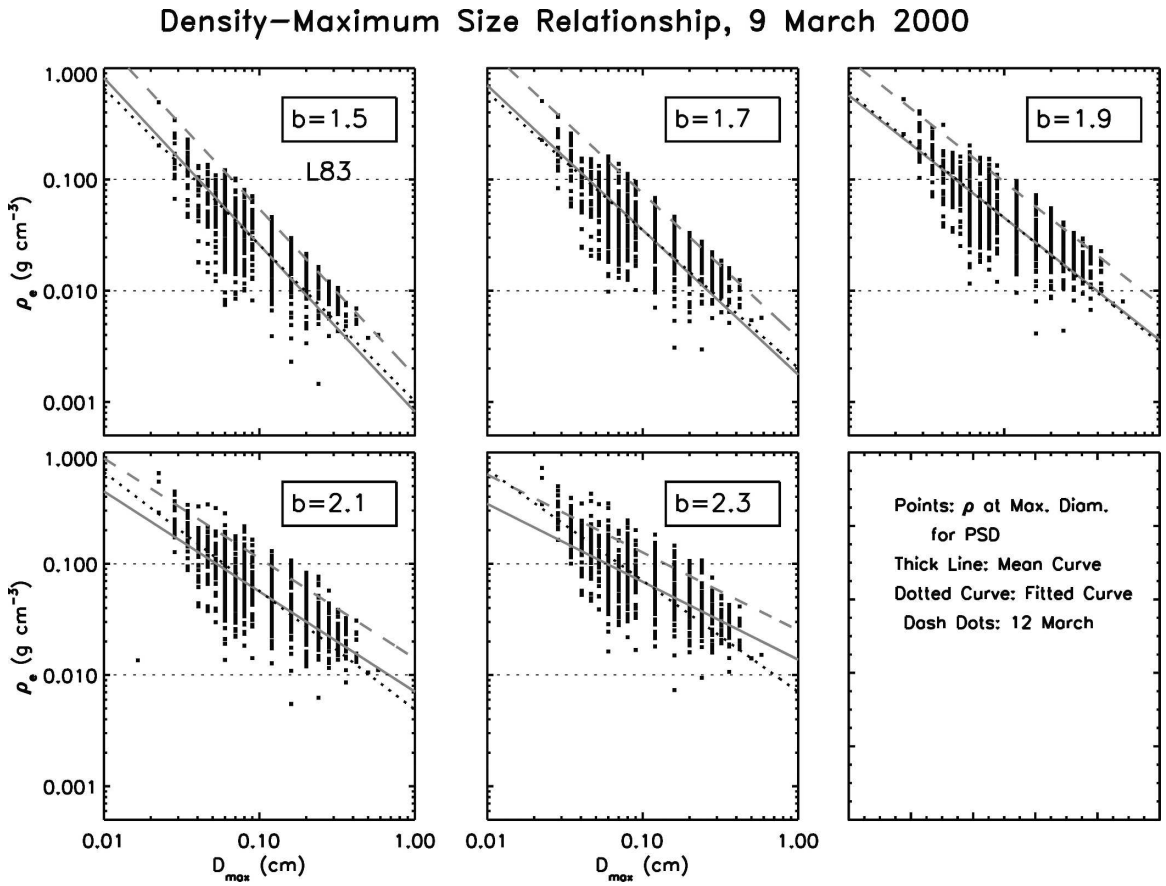

FIG. 7. For 9 March cirrus: particle bulk density (see text) for maximum measured size for each PSD. The solid line in each panel is the mean curve given by ρ_e, the dotted line a fit to the data, and the dashed line the ρ_e–D relationship from the mean a values for 12 March. For 9 and 12 March, the logarithmically weighted, mean density–size relationship is also plotted. Also shown is the mean density from Lin et al. (1983), and a horizontal line at 0.01 g cm^{-3} added for reference.

temperature. For the CRYSTAL FACE data there is a marked temperature dependence. Here, because at all temperatures the particles are mixtures of complex types and because the PSD broaden with temperature, the decrease in ρ_e with temperature basically reflects a shift to larger particle sizes and not to changes in the coefficient a. The ρ_e for the synoptic sizes is different. At and below −20°C, where bullet rosettes and complex spatial crystals predominate, ρ_e is relatively constant at 0.2 g cm^{-3}. In the figure, the points with ρ_e close to 0.2 g cm^{-3}, extending to −10°C, are from the 12 March case in which these crystal forms predominated. The ρ_e above −10°C are from the case on 19 November and are dominated by needles and needle aggregates. The transition region between both extremes indicates types of planar crystals. From the curve fits to the data in Fig. 8, it may be concluded that for microphysical parameterizations, ρ_e can clearly be improved by adding temperature dependence (using the results shown in Table 1).

c. *Sensitivity of ice particle terminal velocities to mass dimensional relationship*

This section examines the sensitivity of single particle and ensemble mass and reflectivity-weighted fall speeds, V_m and V_Z (related to higher moments than the IWC), to the coefficient a given in section 3a. This evaluation will aid in assessing the magnitude of the errors occurring in being able to narrow down the value for exponent b. In addition to particle mass, terminal velocity calculations require an estimate of its cross-sectional area and drag coefficient.

1) CROSS-SECTIONAL AREA

In normal operational orientations, 2D and HVPS imaging probes directly measure cross-sectional areas. Each particle in a size bin has a characteristic area ratio, A_r, the particle area measured by occluded pixels, A_c, divided by the area of an equivalent, maximum diameter sphere. For each 5-s PSD, an average A_r was found

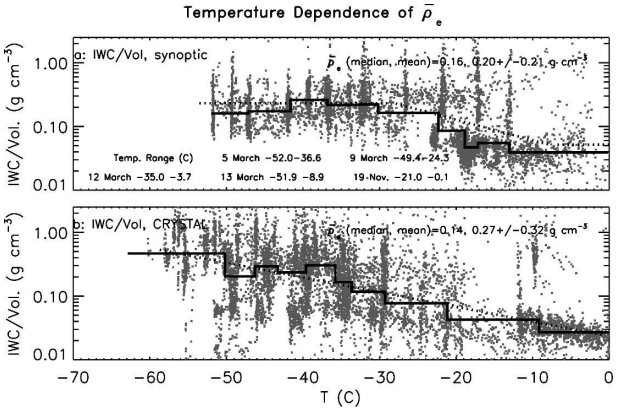

FIG. 8. Ensemble mean effective densities for ice particle populations as a function of temperature: (a) synoptic cases, (b) CRYSTAL FACE. Median values for ρ_e as a function of temperature and fit coefficients from Table 1 are plotted.

for particles in each size bin. To these average A_r, a curve

$$A_r = \gamma D^{\sigma}, \quad A_c = \frac{\pi}{4}\gamma D^{\sigma+2} \tag{3}$$

was fitted to the data, where γ and σ are fit coefficients. For particles in the FSSP size range which are not included in the curve fit and where A_r in Eq. (3) exceeds 1.0, A_r is set to 1.0. On the right side of Eq. (3), the coefficient, $\sigma + 2$, was found to increase systematically with increasing temperature, from a mean of 1.65 at −60°C, 1.70 at −40°C, 1.77 at −20°C, and leveling off at 0°C to 1.81. Probe resolution does not appear to have major effect on this result. For the 9 March case, Heymsfield and Miloshevich (2003) showed, for D above 0.03 cm, $\sigma + 2 = 1.70$ ($\gamma = 0.164$). For the higher resolution CPI and for D above 0.004 cm, they found $\sigma = -0.27$, $\sigma + 2 = 1.73$ ($\gamma = 1.69$). For the CRYSTAL FACE data reported herein, $\sigma + 2$ varies similarly with temperature. These results are shown in more detail in Part II.

2) Calculation of terminal velocity

Theoretical considerations give the terminal velocity of most ice and snow crystals as being a function of the product of three terms: the ratio of particle mass to area, the diameter, and a pressure dependent term $f(P)$ (see H03). To a first approximation [Mitchell 1996, his Eq. (20)],

$$V_t \propto \left(\frac{m}{A_c}\right)^{0.6} D^{0.3} f(P). \tag{4}$$

Earlier observational and modeling studies have represented the terminal velocity of an ice particle of maximum dimension D as

$$V_t = A_0 D^B \left(\frac{P_0}{P}\right)^{\kappa} = AD^B, \tag{5}$$

where A is the intercept, with a value A_0 at 1000 hPa, and B the exponent (L83; RH84). The value of κ is usually given as 0.4 or 0.5 (RH84 and L83, respectively).

The terms A and B are given analytically in Mitchell (1996) as

$$A = a_1 \nu^{1-2b_1} \left(\frac{8ag}{\rho_a \pi \gamma}\right)^{b_1}, \quad \text{and} \tag{6}$$

$$B = b_1(b - \sigma) - 1, \tag{7}$$

where a_1, b_1 are related to the drag coefficient, ν (kinematic viscosity), ρ_a (air density) to the thermodynamics, a and b are the coefficients in the mass dimensional relationship, γ and σ are coefficients in the area ratio dimensional relationship, and g is the gravitational acceleration constant.

3) Size-dependent fall speeds

From Eqs. (6) and (7), terminal velocity is dependent upon the values of a and b. The calculated V_t may vary therefore, even if the IWC, derived from a, b, and PSD, matches the IWC measured by the CVI. This may be illustrated using observations from 9 March: mass is derived using the a coefficient for each b (Fig. 4a); average σ and γ from Heymsfield and Miloshevich (2003); and V_t from drag coefficients from Mitchell and Heymsfield (2005). The size-dependent ratio of particle mass to area for different b is given in Fig. 9 and V_t is a function of this ratio [Eq. (4)]. Sphericity is assumed for FSSP particles and, initially, (m/A_c) will fall along the sloping line for solid ice spheres. For a given value for b and cross-sectional area from Eq. (3), as particle size increases each m/A_c curve on a log–log plot will have a constant slope. At a diameter of about 200 μm, m/A_c is nearly independent of b. As D increases, the curves rapidly diverge and those with the highest b have the highest m/A_c. Even though IWC is reproduced for each average (a, b) pair, as shown in Fig. 10, V_t varies considerably with b.

A simple example, using the 9 March data, is used to illustrate how b affects the mass and reflectivity-weighted fall speeds, V_m and V_z, respectively. The V_m are derived from

$$V_m = \frac{\sum_{i=1}^{n} N_i m_i V_{ti}}{\sum_{i=1}^{n} N_i m_i}, \tag{8}$$

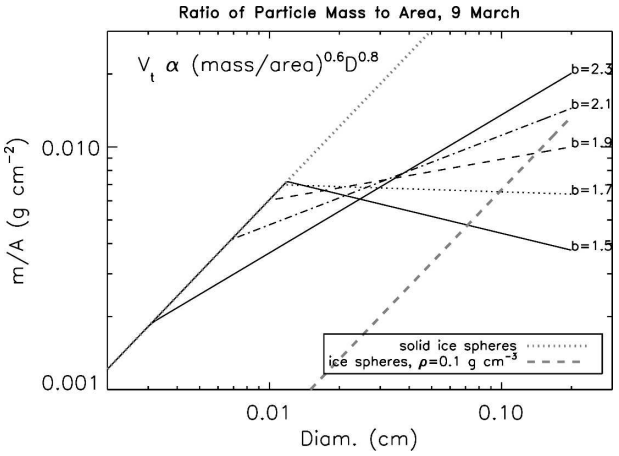

FIG. 9. For 9 March cirrus: ratio of particle mass to area, calculated using derived mean mass and area coefficients. Sloping gray curves, spherical particles with densities of 0.9 and 0.1 g cm^{-3}. Dark curves, ratios for different values for exponent *b*.

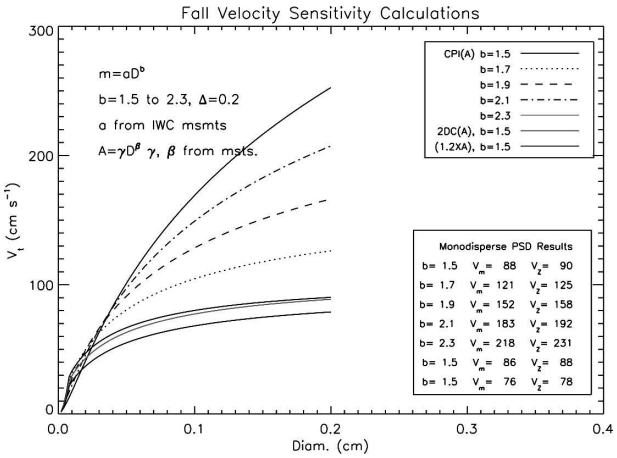

FIG. 10. Calculated, size-dependent, terminal velocities for cirrus crystals from 9 March. Curves show results from different values for *b;* (lower right) mass and reflectivity-weighted fall speeds, derived assuming a constant concentration for all sizes.

where N_i is the concentration of particles in size bin i and the denominator is the IWC; V_Z is similarly calculated. Mass is replaced by its square, IWC by Z_e in units of mm^6 m^{-3}, and the term multiplied by a constant. In this case, the particles size parameter $x(x = \pi D/\lambda$, $\lambda =$ wavelength) is relatively small for all sizes and Mie scattering effects are minimal. To isolate the effect of mass variability, the simplifying assumption is made that the PSD are flat (i.e., N_i is constant for all sizes). Because particle concentration is in both the numerator and the denominator (through IWC), the calculations only show the effect of mass and reflectivity weighting and are informative. In Part II, V_m is derived from measured PSD. The lower panel in Fig. 10 indicates how the choice of exponent *b* profoundly affects ensemble fall velocities, especially V_Z. Particularly in large sizes, this is a consequence of the variation in particle density, mass to area, and fall speed with *b*.

4. Ensemble fall speeds

H03 presented values for coefficient *A*, the terminal velocity of a 1-cm ice particle, and exponent *B*, the rate of increase in the fall velocity with size, in terms of the slope, λ, of fitted gamma-type PSD. This work is extended here by examining the variability of *A* and *B* to the coefficient *b* and to the temperature.

For each 5-s interval, particle mass and mean area per size bin, temperature, and pressure are used to derive the distribution of V_t with *D*. Mass was based on the temperature-dependent (average) mass coefficient *a* from Fig. 6 and Table 1, because V_t values could be obtained where IWCs are <0.01 g m^{-3}, of importance at the lower temperatures. The V_t–*D* relationship was ordinarily linear (on a log–log scale) above about 150 μm, and a power-law curve fitted to the data gave *A* and *B*.

Figure 11 shows that *A* and *B* (for pressure at the measurement level) decrease with increasing temperature for the synoptic cases. At the warmest temperatures, *A* is in the range of about 130 to 300 cm s^{-1} near 0°C, which is comparable to what is expected for 1-cm aggregates. As temperature increases, the maximum particle size increases. The decrease in *B* with temperature signifies that the rate of increase of V_t slows with increasing size. This result is for two reasons: drag-law (Reynolds number–best number) considerations [see Mitchell 1996, his Eqs. (18)–(22)], and because particle density decreases with particle size (Fig. 7).

Although V_t is given by the combination of variables *A* and *B*, we can examine whether the trends with temperature (and pressure) are similar to those employed in earlier parameterizations. In Fig. 11a, a dotted line shows $152(\rho_0/\rho_a)^{0.50}$, which is the coefficient *A* used in the L83 scheme, where ρ_0 is the air density at 1000 hPa and $T = 0$°C and ρ_a is the air density at the observation level. (To find pressure for a given value of the temperature, an average temperature–pressure curve based on the observations is used). Similarly, the *A* coefficient used in the RH84 scheme, $86(P_0/P_a)^{0.4}$ is plotted. Near 0°C, these curves match the calculations reasonably closely but they become increasingly lower than the calculations as temperature decreases. Most importantly, *B* from the earlier studies are too low. H03 presented values for *A* and *B*, for *b* of about 2.3, which are almost the same as those found here.

In Fig. 12, it is noted that the change in the *A* and *B*

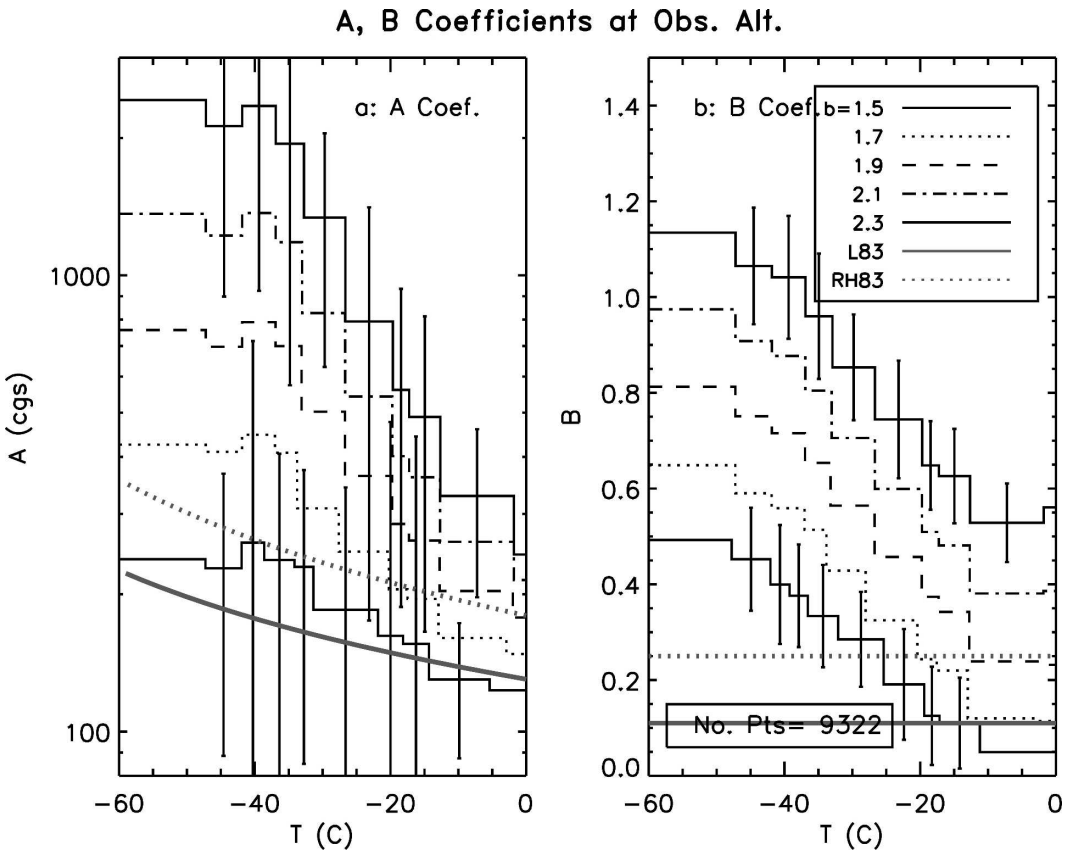

FIG. 11. Temperature dependence of the coefficients A and B for synoptic cases spanning the range of b from 1.5 to 2.1, derived for the observed temperatures and pressures. Values of A and B used by L83 and RH84 one-moment microphysical schemes, adjusted to the observed pressures as described in the text, are shown.

coefficients derived for the CRYSTAL FACE clouds with temperature (at the measured pressure level) is flatter than those found for the synoptic clouds, with higher intercepts at 0°C. These trends are largely due to the greater uniformity in the maximum particle sizes and masses over the full range of temperatures, and the higher densities (and therefore the V_t) of the larger particles. The coefficients for the L83 and RH84 schemes fit these observations better than for the synoptic cases. The data converge on a common value of A near 0°C of 300 cm s^{-1} (Fig. 12a), corresponding to V_t of a 1-cm particle falling at a mean pressure of 580 hPa, and are higher than for the synoptic cases.

Air density has an approximately 75% effect on the V_t over the range of the conditions sampled here; this can be seen from the change in the A coefficients for the L83 and RH84 parameterizations plotted in Figs. 11 and 12. To a first approximation, the density effect is given by

$$\frac{A(P)}{A(1000\ \text{hPa})} = \left(\frac{\rho_0}{\rho_a}\right)^{\kappa}. \tag{9}$$

Although Eqs. (6) and (7) can be used to derive the dependence on ρ_a explicitly, modern weather forecast models [e.g. Weather Research and Forecasting (WRF)] still use Eq. (9) [actually, $(1000/P)^{\kappa}$] to correct the terminal velocities relative to their values at a reference level. This correction method is more computationally efficient than using Eq. (6). Because until now κ has been estimated ad hoc, it is important to quantify its value. In Fig. 13a, the ratio $A(P)/A(1000\ \text{hPa})$ is plotted as a function of $(\rho_0/\rho_a)^{0.54}$, where ρ_a is derived for pressure levels from 200 to 700 hPa in increments of 100 hPa, using the mean temperatures corresponding to the measurements, and these values are compared to A at 1000 hPa; a 1:1 relationship means that κ is approximately 0.54. The estimates shown in Fig. 13 span the full range of b from 1.5 to 2.3; there is a slight downward movement of κ with increasing b, accounting for the spread of the points around the line in the figure; B given by Eq. (7) is pressure dependent is because b is a function of temperature (Fig. 6) and in our calculations temperature and pressure changes are linked. The deviation noted in the higher values of the abscissa is for

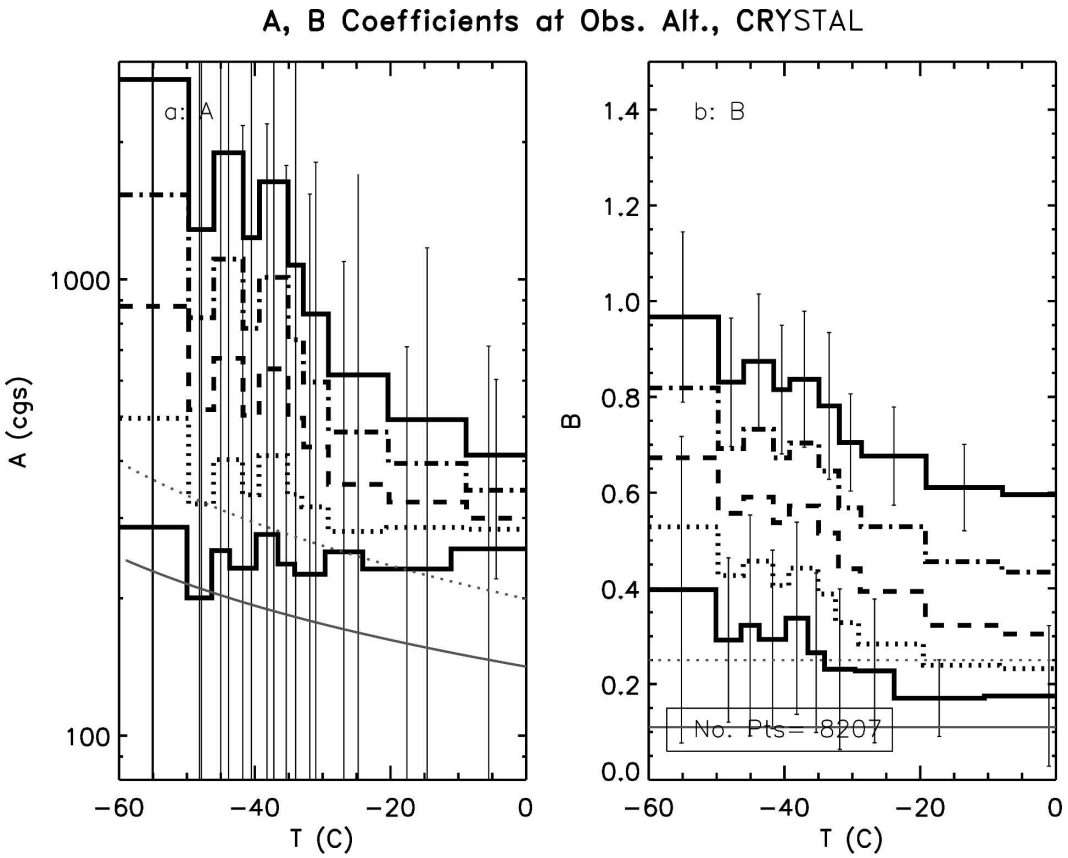

FIG. 12. Same as Fig. 11, except for the CRYSTAL FACE dataset.

the largest b, which are shown in Part II to be overestimates. Although there is some scatter in the data, $\kappa = 0.54$ captures the dependence given by Eq. (9). Similar results are found for the CRYSTAL FACE dataset. H03 found κ ranged from 0.51 to 0.61 at air pressures between 500 and 250 hPa, respectively, comparable to the dependence found here.

The coefficient B increases slightly with pressure (Fig. 13b), due to the variation of exponent b on temperature (and hence atmospheric pressure). This effect is largely independent of B and is characterized for all values of b in Fig. 12b

The V_t–D relationship for particles below 150 μm is sufficiently different than above it and due to the importance of V_t on cirrus cloud persistence proper consideration rather than extrapolation of the results in Figs. 11 and 12 is warranted. In Fig. 14, the temperature dependence of the A and B coefficients in small particle sizes are plotted for two values of b and at two pressure levels that span a wide range of conditions. The B values are large and almost independent of the temperature, and the A values largely reflect the quantitative values of b. For example, a 100-μm particle at a temperature of -60°C and pressure of 300 hPa, with $A = 1.6e5$ and $B = 1.8$, will fall at 40 cm s^{-1} and for a pressure of 1000 hPa, will fall about 66% faster. It is clear that the exponent B from the L83 and RH84 schemes do not conform to the large value of B found for small particles.

5. Discussion

This section contains evaluation of the average temperature-dependent relationships for a in Table 1 as to whether they produce accurate IWCs and whether the findings may be explained analytically from knowledge of how the properties of PSD vary with temperature.

The temperature dependence of q, defined as the ratio of the calculated IWC to that measured by the CVI, is given in Fig. 15. In this figure, exponent b is taken as 1.9 to conform to the BF95 exponent and a from the temperature-dependent coefficients shown in Table 1. For the synoptic cases and all values of b, the IWC is accurately derived and demonstrates that the coefficient a is indeed temperature dependent. The complexity of the particles and their variability on

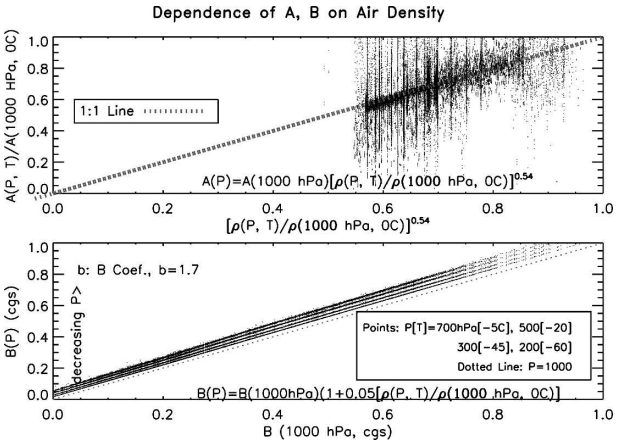

FIG. 13. (a) Ratio of A at pressure levels ranging from 200 to 700 hPa to the value at 1000 hPa, a function of the ratio of air density at 1000 hPa to that at the pressure level to the power of 0.54. Mass coefficient b spans the range of 1.5 to 2.1 and a coefficients are those derived from the temperature-dependent averages. (b) Same as (a) except for coefficient B, for a mass exponent value of 1.7. Other values of b showed similar tendencies.

12 March and 19 November indicates that reliable estimates of the IWC at temperatures above −20°C might require knowledge of the particle types within the layer; this could be estimated from cloud top height, for example. For the 7900 points for the synoptically generated clouds, the average value of q for $b = 1.9$ is 0.97 the median value is 0.91, 30% of the points are between 0.8 and 1.2, and 55% are between 0.6 and 1.4. The results are similar for other values of b.

The ratio q for exponent b of 1.9 is shown in Fig. 16, using the BF95 value for a. Here, for temperatures above −20°C, the mass dimension relationship reproduces the measured IWC reasonably well but clearly does not do so at lower temperatures.

Figure 17 shows the IWC derived from the $m(D)$ parameterization for the CRYSTAL FACE PSD. Here, b is taken to be 1.9. The parameterization does an excellent job of representing the IWC for all temperatures. For the 8700 in situ data points, the average value of q is 1.18, the median is 0.98, 44% of the points are between 0.8 and 1.2, and 71% are between 0.6 and 1.4.

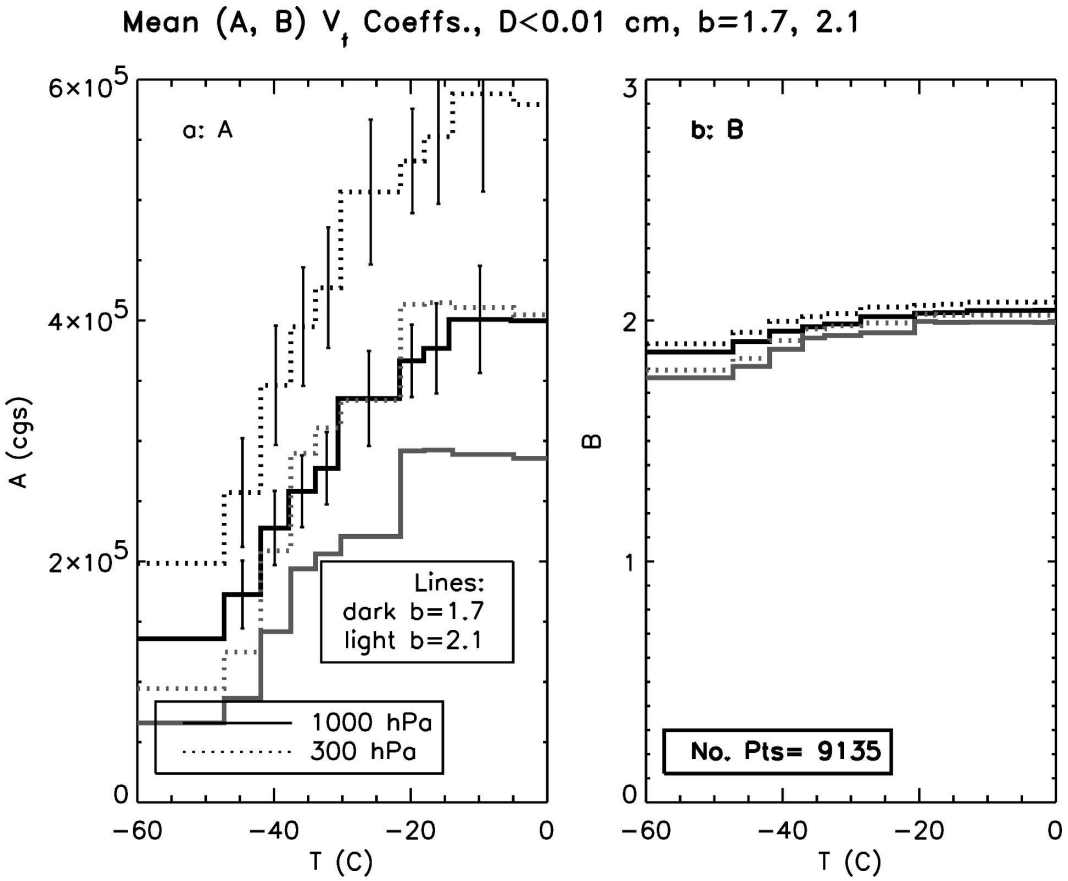

FIG. 14. Same as Figs. 11 and 12, except that the coefficients are derived for particles below 100 μm in diameter.

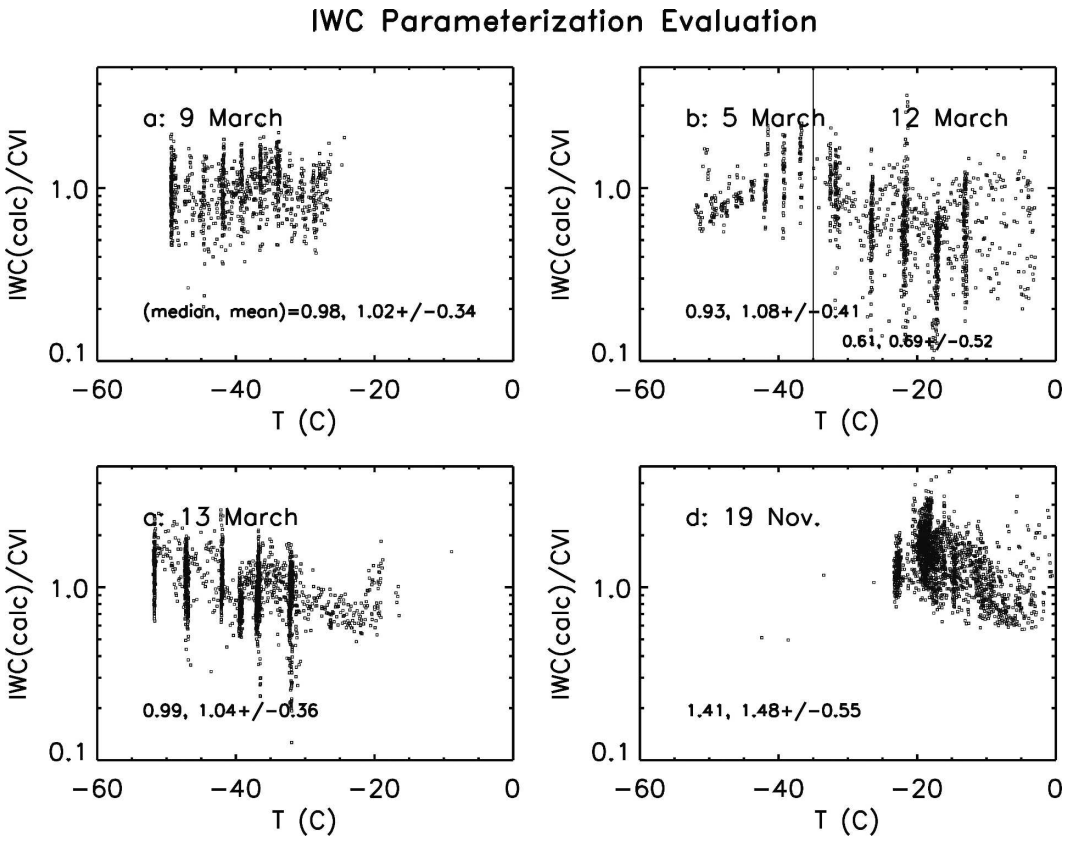

FIG. 15. Median and mean values for the ratio (q), for IWC, calculated using $b = 1.9$ with the temperature-averaged a coefficients and divided by the IWC measured above its detection limit by the CVI.

The increase in a with temperature may be explained by analytic integration of gamma PSDs. The IWC is given by

$$\mathrm{IWC} = \int_0^\infty N(D)m(D)\,dD, \tag{10}$$

where $N(D)$ is the size-dependent concentration. If $N(D)$ is represented by a single gamma distribution of the form

$$N(D) = N_0 D^\mu e^{-\lambda D}, \tag{11}$$

where N_0 is the intercept, λ the slope, and μ the dispersion, then

$$\mathrm{IWC} = aN_0 \int_0^{D_{\max}} D^{b+\mu} e^{-\lambda D}\,dD = aN_0 \frac{\Gamma(b+\mu+1)}{\lambda^{(b+\mu+1)}}. \tag{12}$$

After H04, the equivalent spherical volume of the ice particle population is given by

$$\mathrm{V} = \frac{\pi}{6} N_0 \int_0^{D_{\max}} D^{3+\mu} e^{-\lambda D}\,dD \approx \frac{\pi}{6} N_0 \frac{\Gamma(4+\mu)}{\lambda^{(4+\mu)}}, \tag{13}$$

where $D_{\max}$ is taken to be ∞. Therefore,

$$\overline{\rho_e} = \frac{\mathrm{IWC}}{V}. \tag{14}$$

Rearranging,

$$a = \frac{\pi}{6}\overline{\rho_e}\frac{\Gamma(4+\mu)}{\Gamma(b+\mu+1)}\lambda^{b-3}. \tag{15}$$

As λ and μ both decrease with temperature, the net effect on a is not readily ascertained. Figure 18a, for the synoptically generated ice cloud cases, shows the coefficient a as a function of temperature for two values of b. An analytically derived value for a may be derived using the gamma fit coefficients for PSD as given in H04 and in references cited in the article, and the $\overline{\rho_e}$ from Fig. 7 herein. As shown in Fig. 18b, the corresponding values for a, as derived from Eq. (14), closely

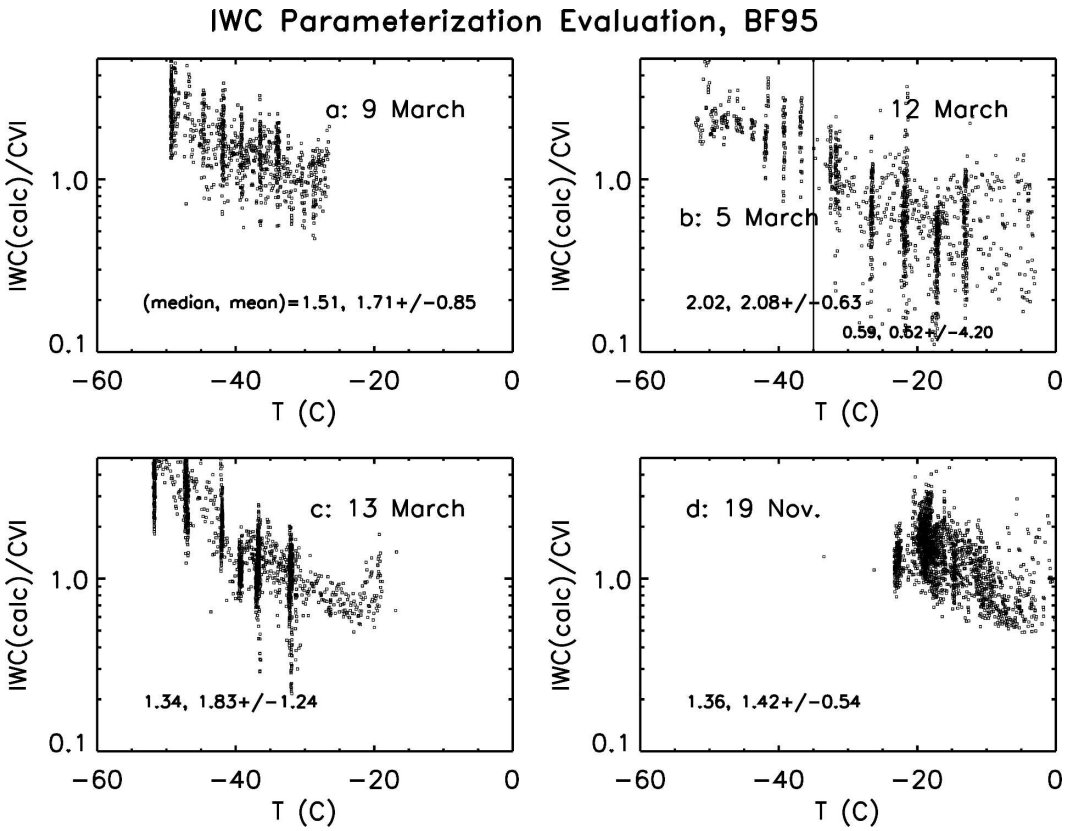

FIG. 16. As in Fig. 15, using the BF95 coefficient: $a = 0.002\,94$ (cgs).

fit the observations, indicating that a's temperature dependence is a result of how the properties of PSD and $\overline{\rho_e}$ vary with temperature. The aggregation process is fundamental to this result, which, as the temperature increases, broadens the PSD.

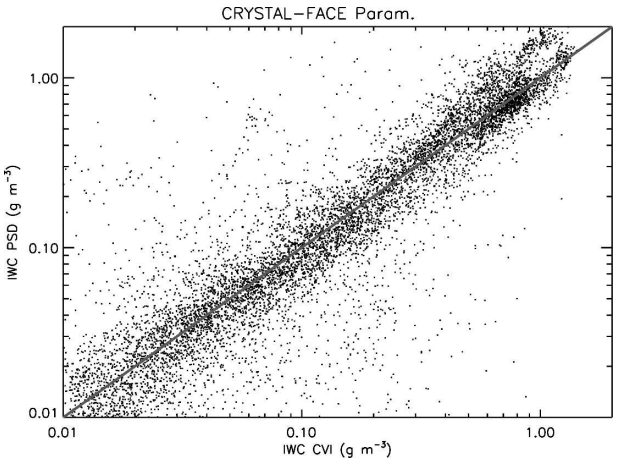

FIG. 17. IWC calculated from the PSD vs those measured by the CVI for CRYSTAL FACE clouds. The exponent b is 1.9, and the 1:1 line is shown.

The result is similar in convectively generated cirrus where H04 have shown that $\overline{\rho_e}$ increases with λ and decreases with temperature. The mixing associated with deep convection tends to homogenize ice particle populations primary through upward transport in vertically deep updrafts, thus accounting for a being relatively independent of temperature. Sedimentation of the large crystals in anvils would tend to further homogenize the populations.

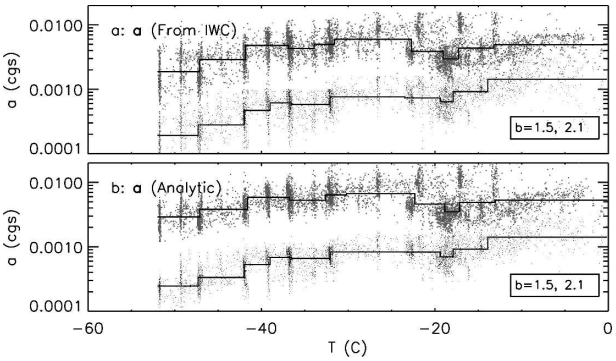

FIG. 18. (a) Derived and (b) calculated temperature dependence for the a coefficient using two values for exponent b.

6. Summary and conclusions

Part I of this two-part study uses particle size distribution and condensed water content measurements in mid- and low-latitude ice clouds to find single, power-law mass dimensional relationships $m = aD^b$, with b ranging from 1.5 to 2.3, covering the full size distribution and giving accurate IWC. The results are used to develop ice particle fall velocity expressions in terms of exponent b, particle diameter, and air density. The motivation for this research is to develop accurate estimates of the mean mass weighted fall speed of ice particle populations, central to the understanding of ice cloud extent and longevity. A single power law is desirable to simplify analytical specification of a range of moments. Part I finds the a coefficients that produce the measured IWC over the full range of values for exponent b. Using the (a, b) values that produce the correct IWC, the calculated ice particle fall velocities are found to vary by more than 20%. Part II will refine estimates of the exponent b coefficient and provides quantitative values for a, and the associated fall velocity expressions for use in cloud and climate models.

For temperatures from −60° to 0°C, coefficient a is found to increase with habit, especially at temperatures above −20°C, playing a significant role for the synoptic cases. Scatter at the warmer temperatures is due to habit variability. The relative absence of a temperature dependence for the convective (CRYSTAL FACE) cases reflects the point that vertical transport tends to dampen habit variability.

The temperature dependence of the a coefficient may be accounted for analytically and may also be explained by the way ice crystals nucleate and grow. At the small end of a single power-law type $m(D)$ relationship, which we show fits the observations, one anchor for the $m(D)$ relationship is given by the point at which an ice particle begins to take on a nonspherical shape and its mass is less than that of an equivalent diameter sphere. This occurs at the threshold diameter where the density implied by the $m(D)$ relationship equals 0.91 g cm^{-3}: $D_t = (6a/0.91\pi)^{[1/(3-b)]}$. Below this size the density is approximately 0.91 g cm^{-3}. From the theory of homogeneous nucleation we know that at the point of nucleation, the lower the temperature, the smaller the cloud drop or the haze particle. This is supported by high-resolution images of small ice particles (e.g., Heymsfield 1986) that suggest that the lower the temperature, the smaller D_t. Drop sizes frozen by heterogeneous nuclei are also likely to diminish with temperature. In any event, decreasing a with temperature implies a decreasing D_t. The largest particles in a distribution give an anchor point at the large end of the PSD. Many observations show maximum particle size increasing with temperature; therefore, the anchor point at the large end of the PSD increases with temperature. A single $m(D)$ relationship shifts, therefore, to higher a with increasing temperature. Brown and Francis (1995) reported a single, relatively large value of $D_t = 90$ μm for synoptically generated ice cloud layers but it cannot be considered applicable to ice clouds in wide temperature ranges. Evaluation of the dependence of D_t on cloud type, mode of nucleation, and temperature is likely to be a primary factor in what controls mass dimensional relationships. What is clearly needed for this, especially for low temperatures, are instruments with resolutions superior to the cloud particle imaging probe.

Another important result of this study is the finding that the mean effective density for ice particle populations, $\overline{\rho_e}$, may also be represented in terms of temperature. This is in contrast to the reports of L83 and RH84 who take the ensemble mean density to be a constant 0.1 g cm^{-3}. It has been found that, for cirrus populations formed by large-scale uplift, at −25°C and below $\overline{\rho_e}$ is nearly constant at 0.2 g cm^{-3}. This diminishes with increasing temperature, reflecting the predominance of particles with lower densities: planar crystals, needles, and aggregates of such particles. There is a progressive decrease in $\overline{\rho_e}$ with temperature in ice clouds formed by convective updrafts that reflects the broadening of the size distribution to include low-density aggregates. From −20 to 0°C, $\overline{\rho_e}$ diminishes from about 1/2 of 1/4 of the Lin et al. (1983) value. The effect of these lower densities on precipitation production in numerical models needs to be addressed.

Acknowledgments. The authors wish to thank Paul Field, Hugh Morrison, Carl Schmitt, Gerd-Jan van Zadelhoff, David Donovan, Anthony Illingworth, and Robin Hogan for valuable discussions. The efforts of Mike Poellot, who organized the data collection for the Citation flights, are greatly appreciated. Access to the AIRS-2 C130 data through John Hallett and Jeffrey Stith is appreciated. The authors also wish to thank Nancy Knight for editing the manuscript. This research was supported in part through the NASA CRYSTAL program, Grant NNH04AA821, Hal Maring, Program Manager.

APPENDIX

CVI Accuracy and Uncertainty and Implications

The CVI probe measured the condensed water in cloud particles larger than 6–8-μm diameter, with the

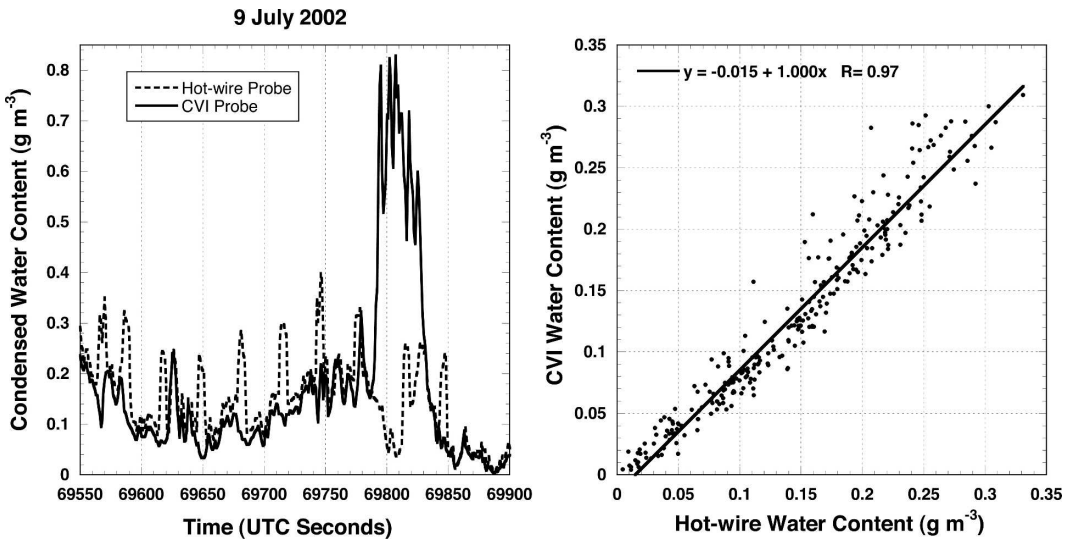

FIG. A1. Cloud water content measured by the CVI and the King hot-wire probe in a primarily supercooled cloud in CRYSTAL FACE on 9 Jul 2002.

precise value depending on the aircraft and airspeed. Droplets or ice crystals were separated from smaller particles and interstitial gases, then impacted into heated dry nitrogen gas. The inlet diameter was 0.635 cm. After evaporation, water vapor measured by a Lyman-alpha or tunable diode absorption hygrometer was used to determine the original cloud condensed water content. These instruments were calibrated for a range of water contents using a Licor LI-610 dewpoint standard. The CVI cut size has been measured by various techniques (e.g., Noone et al. 1988; Anderson et al. 1993; Schwarzenbock and Heintzenberg 2000) and found to agree with theoretical predictions. Since a number of studies have shown that ice crystals smaller than 10 μm are quasi-spherical and have relatively high densities, the cut size in ice clouds should be similar to that in water clouds.

Figure A1 shows a comparison of cloud water content measured by the CVI and the King hot-wire probe in a primarily supercooled cloud in CRYSTAL FACE on 9 July 2002. The hot-wire probe is well characterized and has been shown to be accurate for a wide range of liquid water contents with median volume diameters (MVD) up to at least 32-μm MVD (Strapp et al. 2003). This particular cloud had a MVD of about 30 μm, which should be within the useful measurement range of both the CVI and the hot-wire. In the left-hand side plot, a regular oscillation in the aircraft analog signals led to the periodic peaks seen in the hot-wire signal. Also, substantial large ice crystals were observed by the 2D-probe and produced the much higher CVI signal during the time period from 69 790 to 69 840 s. All these time periods were removed from the data, and the remaining 1-Hz data are plotted in the right side of the figure. The magnitude of the signals is quite similar and a high correlation is observed between the measurements. A slight bias between the CVI and the hot-wire remains, which is not unexpected, given the uncertainties. This exercise confirms that the CVI measures accurately in liquid clouds and therefore that the Lyman-alpha calibration is valid. Additionally, the CVI liquid water content measurements have been shown to agree within the expected uncertainty relative to reference standards used in the NASA icing research tunnel (Twohy et al. 2003). While suitable standards for ice clouds do not exist, since the CVI measures water directly (as vapor) and no assumptions about particle phase, shape or size distribution are required, it is also expected to be accurate for ice clouds. CVI measurements of IWC compare well with those measured by well-characterized instruments that utilize different measurement methods, including the Particle Volume Monitor (Gerber et al. 1999) and the Harvard total water content probe (G. Kok 2006, personal communication).

Uncertainty in the CVI measurement is induced by flow and geometry considerations related to the enhancement factor within the CVI (estimated uncertainty of 10%), to calibration and drift factors related to the Lyman-alpha hygrometer (estimated uncertainty of 8%) and to uncertainties in the baseline (estimated uncertainty 0.001 g m^{-3}). Combination of the above uncertainties via accepted engineering methods (Twohy et al. 1997) leads to an overall uncertainty of about 13%

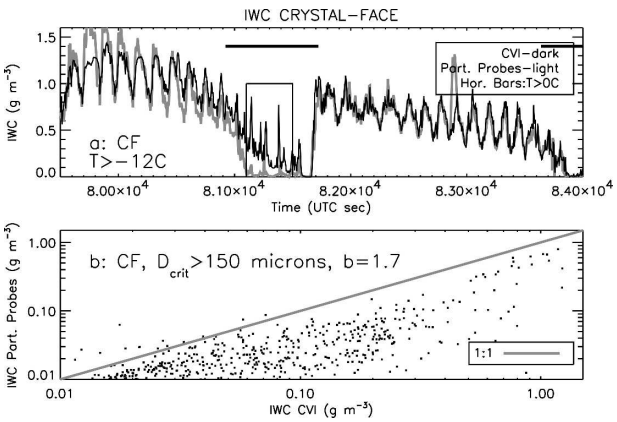

FIG. A2. (a) Ice water content measured by the CVI and derived from the PSD and $a(T)$ parameterization in Table 1, for $b = 1.7$, for two Lagrangian spiral descents on 26 Jul 2002 during CRYSTAL FACE. Rectangular area shows region where there appears to be significant CVI hysteresis. (b) Measured IWC vs that derived from the PSD with $b = 1.7$, for CRYSTAL FACE, when the deduced values of a from the PSD and CVI IWC have a solid ice diameter D_t of >150 μm.

at water contents of 0.05 to 1.0 g m^{-3}. Above 1.0 g m^{-3}, the humidity in the instrument can reach saturation values unless nitrogen flow rates are increased to compensate. Uncertainty increases to 16% at 0.01 g m^{-3}, and to >40% at 0.0025 g m^{-3}. The increase in the uncertainty at lower condensed water contents is due to variations in the out-of-cloud baseline signal from the Lyman-alpha hygrometer as well as artifacts due to hysteresis in the sample lines from prior high IWC cloud passes. Special processing can minimize these effects for individual cloud passes, but are impractical to apply to the dataset as a whole. Therefore, a CVI detection threshold of 0.01 g m^{-3} was used in this paper to mitigate this effect.

Figure A2a illustrates an extreme IWC situation from CRYSTAL FACE, where the Citation made two Lagrangian spiral descents through a cloud layer from −12°C to above 0°C. We use the $a(T)$ parameterization for $b = 1.7$ from Table 1 to derive the IWC. It can be inferred from the figure that the CVI may have underestimated the IWC by ~15% in the regions of peak IWC (>1.3 g m^{-3}) due to saturation and overestimated the IWC in the strong dips due to hysteresis, consistent with the discussion above. Furthermore, the $a(T)$ parameterization appears to work well.

CVI and particle probe errors can lead to errors in the estimated values of the a coefficient, for a given b, derived from the PSD. The mass of particles, for given a and b can exceed the mass of solid ice spheres below a given size D_t, implying that the particles are solid ice spheres or drizzle. The BF95 relationship, with $b = 1.9$, gives $D_t = 90$ μm. This is reasonable and a comparable or lower value was found for the synoptic dataset. Eighteen percent of the CF dataset, with $b = 1.5$, however, had $D_t > 150$ μm, the percentage decreasing to 13% at $b = 1.7$ and 12% at $b = 2.3$. In the CPI imagery, 150 μm liquid or frozen drops were rarely seen, so these were clear instances when there may have been measurement errors.

In Fig. A2b, we show those periods for CRYSTAL FACE when the CVI measured IWC above its detection threshold and the deduced $D_t > 150$ μm, with $b = 1.7$. We can estimate the IWC from the PSD and the parameterization given in Table 1. This is shown on the ordinate, for $b = 1.7$. Because in the mean, the parameterization works well for all IWC (e.g., Fig. A2a), we attribute many of the points where $D_t > 150$ μm to be due to overly large values of the measured IWC, due to hysteresis. For these reasons and also based on the CPI images, those periods in which $D_t > 150$ μm were unused.

REFERENCES

Anderson, T. L., R. J. Charlson, and D. S. Covert, 1993: Calibration of a counterflow virtual impactor at aerodynamic diameters from 1 to 15 μm. *Aerosol Sci. Technol.,* **19,** 317–329.

Atlas, D., S. Y. Matrosov, A. J. Heymsfield, M. D. Chou, and D. B. Wolff, 1995: Radar and radiation properties of ice clouds. *J. Appl. Meteor.,* **34,** 2329–2345.

Baker, B., and R. P. Lawson, 2006: Improvement in determination of ice water content from two-dimensional particle imagery. Part I: Image-to-mass relationships. *J. Appl. Meteor. Climatol.,* **45,** 1282–1290.

Brown, P. R. A., and P. N. Francis, 1995: Improved measurements of the ice water content in cirrus using a total-water probe. *J. Atmos. Oceanic Technol.,* **12,** 410–414.

Field, P. R., A. J. Heymsfield, and A. Bansemer, 2006: Shattering and particle interarrival times measured by optical array probes in ice clouds. *J. Atmos. Sci.,* **23,** 1357–1371.

Fowler, L. D., D. A. Randall, and S. A. Rutledge, 1996: Liquid and ice cloud microphysics in the CSU general circulation model. Part I: Model description and simulated microphysical processes. *J. Climate,* **9,** 489–529.

Gerber, H., G. Frick, and A. R. Rodi, 1999: Ground-based FSSP and PVM measurements of liquid water content. *J. Atmos. Oceanic Technol.,* **16,** 1143–1149.

Heymsfield, A. J., 1986: Ice particles observed in a cirriform cloud at −83°C and implications for polar stratospheric clouds. *J. Atmos. Sci.,* **43,** 851–855.

——, 2003: Properties of tropical and midlatitude ice cloud particle ensembles. Part I: Median mass diameters and terminal velocities. *J. Atmos. Sci.,* **60,** 2592–2611.

——, and J. Iaquinta, 2000: Cirrus crystal terminal velocities. *J. Atmos. Sci.,* **57,** 916–938.

——, and L. M. Miloshevich, 2003: Parameterizations for the cross-sectional area and extinction of cirrus and stratiform ice cloud particles. *J. Atmos. Sci.,* **60,** 936–956.

——, A. Bansemer, C. G. Schmitt, C. Twohy, and M. R. Poellet,

2004: Effective ice particle densities derived from aircraft data. *J. Atmos. Sci.,* **61,** 982–1003.

——, Z. Wang, and S. Matrosov, 2005: Improved radar ice water content retrieval algorithms using coincident microphysical and radar measurements. *J. Appl. Meteor.,* **44,** 1391–1412.

——, G.-J. van Zadelhoff, D. Donovan, F. Fabry, R. Hogan, and A. Illingworth, 2007: Refinements to ice particle mass dimensional and terminal velocity relationships for ice clouds. Part II: Evaluation and parameterizations of ensemble ice particle sedimentation velocities. *J. Atmos. Sci.,* **64,** 1068–1088.

Isaac, G. A., and Coauthors, 2005: First results from the Alliance Icing Research Study II. *Proc. AIAA 43d Aerospace Science Meeting and Exhibit,* Reno, NV, AIAA, AIAA-2005-0252.

Korolev, A., and G. Isaac, 2003: Roundness and aspect ratio of particles in ice clouds. *J. Atmos. Sci.,* **60,** 1795–1808.

Locatelli, J. D., and P. V. Hobbs, 1974: Fall speeds and masses of solid precipitation particles. *J. Geophys. Res.,* **79,** 2185–2197.

Lin, Y.-L., R. D. Farley, and H. D. Orville, 1983: Bulk parameterization of the snow field in a cloud model. *J. Appl. Meteor.,* **22,** 1065–1092.

Magono, C., and C. W. Lee, 1966: Meteorological classification of natural snow crystals. *J. Fac. Sci. Hokkaido Univ., Ser. 7,* **2,** 321–335.

Mitchell, D. L., 1996: Use of mass- and area-dimensional power laws for determining precipitation particle terminal velocities. *J. Atmos. Sci.,* **53,** 1710–1723.

——, and A. J. Heymsfield, 2005: Refinements in the treatment of ice particle terminal velocities, highlighting aggregates. *J. Atmos. Sci.,* **62,** 1637–1644.

Noone, K. J., J. A. Ogren, J. Heintzenberg, R. J. Charlson, and D. S. Covert, 1988: Design and calibration of a counterflow virtual impactor for sampling of atmospheric fog and cloud droplets. *Aerosol Sci. Technol.,* **8,** 235–244.

Rutledge, S. A., and P. V. Hobbs, 1984: The mesoscale and microscale structure and organization of clouds and precipitation in midlatitude cyclones. XII: A diagnostic modeling study of precipitation development in narrow cold-frontal rainbands. *J. Atmos. Sci.,* **41,** 2949–2972.

Schwarzenbock, A., and J. Heintzenberg, 2000: Cut size minimization and cloud element breakup in a ground-based CVI. *J. Aerosol Sci.,* **31,** 477–489.

Strapp, J. W., and Coauthors, 2003: Wind tunnel measurements of the response of hot-wire liquid water content instruments to large droplets. *J. Atmos. Oceanic Technol.,* **20,** 791–806.

Twohy, C. H., A. J. Schanot, and W. A. Cooper, 1997: Measurement of condensed water content in liquid and ice clouds using an airborne counterflow virtual impactor. *J. Atmos. Oceanic Technol.,* **14,** 197–202.

——, J. W. Strapp, and M. Wendisch, 2003: Performance of a counterflow virtual impactor in the NASA icing research tunnel. *J. Atmos. Oceanic Technol.,* **20,** 781–790.

Westbrook, C. D., R. C. Ball, P. R. Field, and A. J. Heymsfield, 2004: Theory of growth by differential sedimentation, with application to snowflake formation. *Phys. Rev. E,* **70,** 021403, doi:10.1103/PhysRevE.70.021403.

Zhang, Z., and Coauthors, 2004: Geometric optics solution to light scattering by droxtal ice crystals. *Appl. Opt.,* **43,** 2490–2499.